



Dynamic response of electromagnetic railgun under time-dependent electromagnetic moving loads



Bao Zhang^a, Yong Kou^{b,c}, Ke Jin^{b,c,*}, Xiaojing Zheng^{a,**}

^a School of Mechano-Electronic Engineering, Xidian University, Xi'an, 710071, Shaanxi, PR China

^b School of Aerospace Science and Technology, Xidian University, Xi'an, 710071, Shaanxi, PR China

^c Key Laboratory of Equipment Efficiency in Extreme Environment, Ministry of Education, Xidian University, Xi'an, 710071, Shaanxi, PR China

ARTICLE INFO

Article history:

Received 15 May 2019

Received in revised form 9 March 2020

Accepted 11 May 2020

Available online 17 May 2020

Handling Editor: A.V. Metrikine

Keywords:

Vibration response

Railgun

Electromagnetic moving loads

Nonlinear finite element model

Fatigue areas

ABSTRACT

The rail vibration of an electromagnetic railgun can affect the contact status between the armature and rails, even causing rail damage. To reveal the dynamic characteristics of a railgun, we investigated the rail vibration of an electromagnetic railgun under different armature motions. The rail is assumed to be a Euler–Bernoulli based beam, and the time-dependent electromagnetic moving loads applied on the rail are considered. By considering the reaction of the magnetic pressure to the rail deformation, a nonlinear finite element model is proposed to study the dynamic characteristics of the railgun rail. The model validation is presented through a comparison of the model predictions with the analytical solution of the rail deflection, and the experimental result of the rail strain. The differences between the dynamics of rail beam under different moving loads are then compared. Moreover, rail vibration features are discussed in detail. The results indicate that the probable fatigue areas of the rail are located where the pulse current reaches its maximum or where the armature approaches its critical speed. The results of these investigations will help improve the design of railguns.

© 2020 Elsevier Ltd. All rights reserved.

1. Introduction

Railgun technology has been widely used in numerous areas such as the military field [1], aerospace industry [2,3], and material testing [4]. An electromagnetic railgun consists of a pair of conductive rails and a sliding armature (projectile). The rails and armature form a sliding short circuit that converts the electrical energy into the kinetic energy of the armature (projectile). The armature can be accelerated to a speed of many kilometers per second. Powered by the electrical energy stored in capacitors or compulsators, a railgun has the advantages of high speed, cleanliness, zero-emission, and high efficiency compared with a conventional propellant gun. However, a variety of technical challenges still exist in the development of railgun technology, including high-speed rail gouging [5], rail wear [6], and arc damage for an armature transition [7]. Although a large number of relevant studies have been published on the subject of railguns, further exploration of the nature of these technical challenges is necessary. For example, rail gouging has been found to be closely related to rail vibration [8]. Rail vibration can affect the contact status, even causing damage between the armature and rails [9]. Such damage not only

* Corresponding author.

** Corresponding author.

E-mail addresses: kjin@xidian.edu.cn (K. Jin), xjzheng@xidian.edu.cn (X. Zheng).

reduces the service life of the railgun, it also affects the armature speed and muzzle angle associated with the railgun shot accuracy. Therefore, a study on the dynamic response of an electromagnetic railgun is important to improve the efficiency of the railgun launches.

To study the dynamic response of an electromagnetic railgun, the rail supported with the barrel insulation and containment material is modeled as a beam sitting on an elastic foundation. With such a beam model, the critical speed of the railgun rail is derived by separating the variables, and the dynamic behavior of a laboratory railgun using cantilevered supports is investigated [10,11]. In addition, the issue of rail deflection varying with physical and mechanical parameters is resolved using a Fourier sine integral transformation and Laplace–Carson integral transformation [12]. However, these results are only applicable to constant magnetic pressure and constant speed of armature motion. The elastic wave of the rail beam and the contact pressure between the armature and rails were analyzed to explore the transient elastic waves as a possible explanation for the transitioning of solid armatures [13,14]. The wave dynamics of the beam foundation systems (such as a railgun) were investigated using a generalized dynamic stiffness method to reveal the actual causes and physical implications of the critical, shear, and bar speeds [15]. The critical speed for armature motion is associated with the damaging resonant regimes. To better understand the transient resonant regimes in a railgun and reduce the effects of the critical speed, a dynamic and strength analysis of the railgun rail was conducted when the load extending over the rail moved at a constant acceleration [16,17]. Moreover, the dynamic behavior of the railgun under different loading amounts was explored through experimental and numerical studies at the French–German Research Institute of Saint-Louis [18–20]. Such studies have significantly improved our understanding of the dynamics of a railgun, although the consideration of the magnetic pressure and armature motion remains insufficiently comprehensive.

More consideration should be given to the magnetic pressure and armature motion to investigate the dynamic characteristics of a railgun. The magnetic pressure in a railgun constitutes a type of time-dependent electromagnetic moving load. When the armature moves with the constant armature speed or acceleration, the rail-vibration response can be analytically solved using transformation methods at a constant magnetic pressure [21,22]. But the armature moves from an at-rest position to the muzzle within a few thousandths of a second along the rail in practice. Thus, the armature motion at a constant speed or constant acceleration is the special case. Furthermore, the rail-vibrations during an actual launch will be significantly different from the case with constant magnetic pressure. Especially, the magnetic pressure will be further changed by the rail-vibration. Therefore, it is difficult to evaluate the dynamic behavior of a railgun rail under time-dependent electromagnetic moving loads.

The dynamics of beams under various moving loads have been broadly researched owing to their extensive applications in engineering, for example, railroads, bridges, gun-tubes, guideways, and overhead cranes. A comprehensive review of such studies is outside the scope of this paper, although a brief review of a few studies will be helpful in investigating the dynamic behavior of a railgun rail. A large number of studies on the dynamic response of a beam subjected to a moving load can be found in the monographs of Frýba [23]. To the best of the authors' knowledge, there are mainly two types of moving loads on a beam described in the literature. One is a single moving load (point load or finite-length load). The other is a periodic moving load (a series of single moving loads). For a single moving load, the analytical solutions to the vibration response of the beams subjected to the harmonic, constant, and random loads with accelerating, decelerating, and constant speeds of motion were given through a modal analysis [24–28]. The free vibrations of simply and elastically supported beams after a single moving load has passed were analyzed to find the speeds for the maximum or zero amplitude of free vibrations [29]. The dynamic behaviors of multi-span beams were also investigated using an eigenfunction expansion or a modal analysis method, and in combination with a direct integration method [30,31]. The vibration characteristics of a double-beam system were also investigated using the classical modal expansion method [32,33]. For the case of a periodic moving load, the problem of dynamic stability and the steady-state response of a single-span beam bridge subjected to inertial loads was studied by Klasztorny et al. [34]. A simple analytical tool for the evaluation of the dynamic behaviors of weakly damped beams was given by Savin [35]. Moreover, the steady-state vibration of a periodically supported beam on an elastic half-space under a single moving load for a railway track was presented by Metrikine and Popp [36]. This work was further improved by considering the effects of the periodic inhomogeneity of the track on its dynamic response and elastic drag [37]. The stability of the train was then studied by modeling the train's bogie and railway track with the oscillator and beam placed on a viscoelastic foundation [38]. The dynamic behaviors of the beams on an elastic or viscoelastic foundation under moving loads are still the key issues to address for resolving numerous engineering problems [39–44].

The dynamics of railgun rail under time-dependent electromagnetic moving loads is studied using the proposed nonlinear finite element model described in this paper. The railgun rail is modeled as a Euler–Bernoulli based beam on an elastic foundation. The time-dependent electromagnetic moving loads (i.e., loads that rapidly extend over space), are a new and unique type of moving loads differing from the single and periodic moving loads used in previous studies. Such moving loads will extend along the rail and change with the rail vibration under a nonlinear pulse current, which reflects the main advantage of our proposed model (i.e., it can account for the nonlinear dependence of the magnetic pressure on the rail deflection). The proposed model can be degenerated to the cases described in previous studies. Those degenerate cases are the special cases obtained by simplifying the armature motion. Both constant speed and varying acceleration of armature motion are taken as special cases in this paper. Moreover, the armature position is obtained by solving the motion equation that depends on the pulse current, which position is given by experimental measurements or assumptions in previous studies.

The remaining part of this paper is arranged as follows: In Section 2 the model framework is described, and the main computational steps used to solve the governing equation are given. In Section 3, model validation of the proposed nonlinear finite element model is conducted by comparing the model results with the analytical solution of the rail deflection, and with the experimental results of the rail strain. In Section 4, the rail-vibration responses are evaluated and discussed under various conditions of solid armature launch. Finally, some concluding remarks are provided in Section 5.

2. Model framework

2.1. Modeling assumptions

The railgun cross-section, railgun rail, and loading are shown schematically in Fig. 1. The railgun cross-section shows the rail and insulator (often made of fiberglass material, called G-10, or a ceramic) wrapped and supported by a containment structure. The insulator insulates the railgun rail from the outside containment. Owing to the symmetry, only a single rail is considered. To better show the model, the positive and negative rails are shown parallel to the horizontal direction of railgun cross-section (up and down positions) in Fig. 1. However, both rails are parallel to the vertical direction of railgun cross-section in practice [11]. Thus, the effect of gravity is not considered.

The following assumptions for the railgun rail beam model are adopted:

- The beams have a rectangular cross-section and are modeled in accordance with the Euler–Bernoulli theory due to the large slenderness ratio (rail length/rail thickness > 150). In addition, no break in contact between the rail and insulator is permitted. The vertical displacement of the beam is equal to that of the insulator, although the horizontal displacement of the rail is disregarded owing to the close support from the insulator.
- The insulator is believed to have an elastic behavior within the load range considered in this study, and thus the elastic behavior of the insulator wrapping the rails is modeled based on a Winkler-type elastic foundation (similar modeling for a railgun can be found in previous studies [10–20]). The Winkler foundation has two limitations. Firstly, the mass of the insulator is disregarded, which may lead to the critical speed being significantly higher than observed in practice. Second, the Winkler foundation ignores the nonlocality of the response of the foundation, which might be inaccurate at very high speeds. Appendix A shows that the effect of the mass of the insulator can be included in the effective mass of the rail for a railgun. Appendix B considers the influence of the foundation response at neighbour points, but the attenuation effects with increasing spatial distance are not considered (i.e. weak nonlocality of the foundation response). In addition, a non-local foundation model will be a systematic-comprehensive work for railguns at a larger shear modulus, which needs further research. The simplest Winkler model is still used in this study owing to its easier use in engineering applications.
- The outside containment wrapping the insulator is modeled as a rigid constraint.
- The load from the dynamic interaction between the rail and armature is ignored. Note that the armature speed significantly exceeds the minimum phase velocity of the beam structure during at least part of the launch, which may lead to dynamic instability of the moving armature [45,46]. First of all, when the effect of the armature inertia, leading to dynamic instability, is considered, the armature should be assumed as a point mass or a finite-size mass that is in continuous contact with the beam. The continuous contact exactly satisfies one of the necessary conditions for instability to take place. However, the armature plays the role that conducts current between two rails in the railgun, and the directions of the displacements of two rails are opposite. Thus, the continuous contact between the armature and two rails cannot be always satisfied in the railgun. The loss of contact events can occur due to rail vibration, leading to drops in the energy supply. Therefore, a continuous energy supply cannot be provided to develop the instability. Second, the experimental results (Fig. 4 of the current manuscript) seem to suggest that dynamic instability does not take place, as the magnitude of the rail vibration closer to the free end of the rail is not larger than that farther away from it [47]. This may be due to a stiffening effect in the support structure, which prevents the instability to further

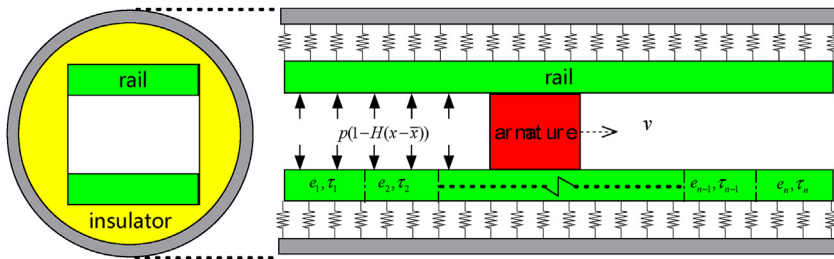


Fig. 1. (a). Schematic of the railgun cross-section, and a beam model of a railgun rail and loading.

develop but does not affect the onset of dynamic instability. The onset of dynamic instability should be considered in a further detailed study. Therefore, the armature inertia, leading to dynamic instability, is not considered in this paper.

The loading is discontinuous at the armature position where the pulse current passes through. The load mainly includes magnetic pressure. The magnetic pressure is present on the rail behind the armature, but is absent from the rail ahead of the armature (see Fig. 1). The magnetic pressure front will follow the armature moving through the railgun barrel. The increases in the range of the moving load distinguishes this study from other studies on the moving load. The rail beam model is equally divided into n elements for finite element analysis, and each element e_i , $i = 1, 2, \dots, n$ is associated with a time step of τ_i , $i = 1, 2, \dots, n$ to obtain the numerical solution conveniently.

2.2. Governing equations

During armature motion, good electrical contact between the rail and armature is necessary to conduct current, and thus the rail is closely supported by the insulator and the deformed angle of the rail beam is small. Moreover, since the railgun rails have a small rectangular cross-section and a large slenderness ratio, the assumption that the “plane sections remain plane” is satisfied, and therefore the railgun rail is modeled using the Euler–Bernoulli beam model. The rail-vibration response is described using Eq. (1) according to the Euler–Bernoulli beam theory, where ρ , A , E , I_m , and k are the density, cross-sectional area, Young’s modulus, cross-sectional moment for rail, and the stiffness for the Winkler-type elastic foundation, respectively; and w and f are the rail deflection and loading applied to the rail. The loading is applied to the rail behind the armature, and thus f is described by the Heaviside step function H and the Dirac delta function δ , which depend on the armature position \bar{x} . The loading is a discontinuous function that includes the contact force F_N and the magnetic pressure p . The contact force and magnetic pressure front will move along the rail at an increasing speed.

$$\rho A \frac{\partial^2 w}{\partial t^2} + EI_m \frac{\partial^4 w}{\partial x^4} + kw = f(I(t), w) \quad (1)$$

$$\begin{aligned} f &= p(I(t), w)(1 - H(x - \bar{x})) + F_N \delta(x - \bar{x}) \\ H(x - \bar{x}) &= \begin{cases} 1 & x \geq \bar{x} \\ 0 & x < \bar{x} \end{cases} \end{aligned} \quad (2)$$

The magnetic pressure p , which is closely related to the pulse current and rail vibration, is derived. A schematic of the pulse current applied to the rails is shown in Fig. 2, where b , h , and r are rail width, rail thickness, and half of the distance between the inner wall of two rails, respectively. When the pulse current I is applied to the rails, the current tends to flow on the inner walls 1 and 2 of the rail owing to the current skin effect.

The current density through each rail wall is as follows:

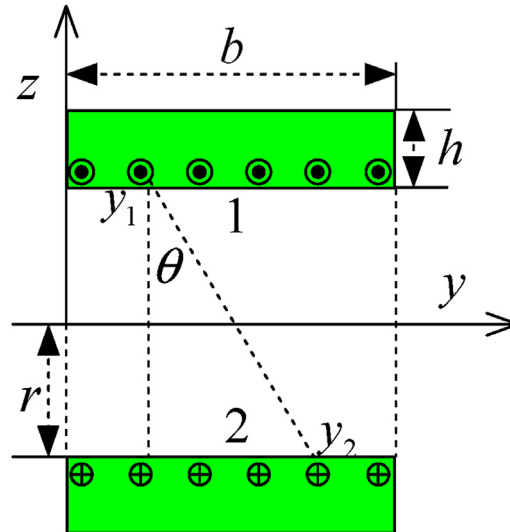


Fig. 2. Schematic of pulse current applied to rails.

$$i_1 = i_2 = \frac{I}{b}. \quad (3)$$

According to the Biot–Savart law of electromagnetics, owing to the symmetry, the magnetic induction intensity of current element dy_1 in wall 1 producing on the current element dy_2 in wall 2 is as follows:

$$B_1 = \frac{\mu_0 i_1 dy_1}{2\pi \sqrt{4r^2 + (y_2 - y_1)^2}}. \quad (4)$$

The repulsive force between the current element dy_1 in wall 1 and the current element dy_2 in wall 2 is as follows:

$$dF_z = B_1 i_2 dy_2 \cos(\theta) = \frac{2r\mu_0 I^2}{2\pi b^2 (4r^2 + (y_2 - y_1)^2)} dy_1 dy_2. \quad (5)$$

Therefore, the magnetic pressure between the rails is as follows:

$$\begin{aligned} p\left(I(t), w\right) &= F_z = \int_0^b \int_0^b dF_z = \int_0^b \int_0^b \frac{2r\mu_0 I^2}{2\pi b^2 (4r^2 + (y_2 - y_1)^2)} dy_1 dy_2, \\ &= \frac{\mu_0 I^2}{2\pi b^2} \int_0^b \left(\arctan \frac{b - y_2}{2r} + \arctan \frac{y_2}{2r} \right) dy_2 \\ &= \frac{\mu_0 I^2}{\pi b} \left(\arctan \frac{b}{2r} + \frac{r}{b} \ln \frac{4r^2}{4r^2 + b^2} \right) \end{aligned} \quad (6)$$

$$r = r_0 + w, \quad (7)$$

$$I(t) = \alpha e^{-\xi_0 t} \sin(\omega t), \quad (8)$$

where μ_0 is the vacuum permeability. The distance between the inner wall of two rails will be changed by rail vibration, and the half distance is equal to the initial half distance r_0 plus the rail deflection w . The pulse current [48] is represented in Eq. (8), in which t , α , ξ_0 , and ω are the time and parameters related to the capacitors, inductors, and resistors of power supply, respectively.

$$ma = f_E + f_N + f_A \quad (9)$$

$$f_E = \frac{1}{2} L' I^2. \quad (10)$$

$$f_N = -2\mu F_N = -2\mu (F_{N,me} + F_{N,em}) \quad (11)$$

$$f_A = \frac{\gamma_a + 1}{2} \rho_{air} \left(A_b v^2 + A_b x a + \frac{1}{2} C_f p_f v^2 x \right) \quad (12)$$

The armature subjected to an electromagnetic force from the pulse current will move. The motion can be described by Eq. (9), in which m and a are the mass and acceleration of the armature, respectively. In addition, f_E is the electromagnetic force (the Lorentz force) accelerating the armature [49] and is represented by Eq. (10), in which L' and I are the inductance gradient and pulse current, respectively, and f_N , as determined through the experimental study by Lee et al. [50], is the frictional drag, and is represented by Eq. (11), in which μ and F_N are the friction coefficient and contact force, respectively. The contact force includes the initial contact pressure $F_{N,me}$ and the transverse component of electromagnetic force $F_{N,em}$ applied to the armature. In addition, f_A is the air drag [51], in which γ_a , ρ_{air} , A_b , C_f , p_f , x , and v are the specific heat ratio, air density, cross-sectional area of the barrel, viscous drag coefficient, perimeter of the barrel, armature position, and armature speed, respectively. The first two components of Eq. (12) dominate the air drag [51].

$$\int_{\Omega} \delta w \left(\rho A \frac{\partial^2 w}{\partial t^2} + EI \frac{\partial^4 w}{\partial x^4} + kw - f \right) d\Omega = 0 \quad (13)$$

With the virtual work principle, the rail-vibration Eq. (1) can be reduced to an equivalent integral form of Eq. (13), in which δw is the virtual displacement and f is the loading.

$$w = \sum_{i=1}^n N_i w_i = \mathbf{N} \mathbf{w}_e \quad (14)$$

The deflection is expressed by the Lagrange interpolation polynomial in Eq. (14), where \mathbf{w}_e is the displacement vector of the element nodes, and one displacement degree of freedom and one rotational degree of freedom occur at each node of the element. In addition, \mathbf{N} is a Hermite shape function matrix. The Hermite shape function matrix and the expressions of the displacement vector of an element can be shown as follows,

$$\mathbf{N} = \left[1 - 3\frac{\xi^2}{l^2} + 2\frac{\xi^3}{l^3} \quad x - 2\frac{\xi^2}{l} + \frac{\xi^3}{l^2} \quad 3\frac{\xi^2}{l^2} - 2\frac{\xi^3}{l^3} - \frac{\xi^2}{l} + \frac{\xi^3}{l^2} \right], \quad (15)$$

$$\mathbf{w}_e = [w_i \ \varphi_i \ w_j \ \varphi_j]^T. \quad (16)$$

The mass matrix \mathbf{M}^e and the stiffness matrix \mathbf{K}^e , as well as the load vector \mathbf{q}^e of the electromagnetic interaction, are obtained by substituting Eqs. (14)–(16) into Eq. (13) for one element, in which l is the length of the element and $\bar{\xi}$ is the relative position of the armature in the rail element

$$\mathbf{M}^e = \frac{\rho A l}{420} \begin{bmatrix} 156 & 22l & 54 & -13l \\ 22l & 4l^2 & 13l & -3l^2 \\ 54 & 13l & 156 & -22l \\ -13l & -3l^2 & -22l & 4l^2 \end{bmatrix}, \quad (17)$$

$$\mathbf{K}^e = \frac{EI}{l^3} \begin{bmatrix} 12 & 6l & -12l & 6l \\ 6l & 4l^2 & -6l & 2l^2 \\ -12l & -6l & 12 & -6l \\ 6l & 2l^2 & -6l & 4l^2 \end{bmatrix} + \frac{kl}{420} \begin{bmatrix} 156 & 22l & 54 & -13l \\ 22l & 4l^2 & 13l & -3l^2 \\ 54 & 13l & 156 & -22l \\ -13l & -3l^2 & -22l & 4l^2 \end{bmatrix}, \quad (18)$$

$$\mathbf{q}^e = \begin{cases} p \begin{bmatrix} l & \frac{l^2}{12} & \frac{l}{2} & -\frac{l^2}{12} \end{bmatrix}^T + F_N \mathbf{N} \left(\bar{\xi} \right), & x \leq \bar{x} \\ p \begin{bmatrix} 0 & 0 & 0 & 0 \end{bmatrix}^T, & x > \bar{x} \end{cases}. \quad (19)$$

The global dynamic governing equation in matrix form is obtained as follows:

$$\mathbf{M} \ddot{\mathbf{w}}(t) + \mathbf{C} \dot{\mathbf{w}}(t) + \mathbf{K} \mathbf{w}(t) = \mathbf{q}(t, \mathbf{w}(t)), \quad (20)$$

where \mathbf{M} , \mathbf{C} , \mathbf{K} , and $\mathbf{q}(t, \mathbf{w}(t))$ are the global mass matrix, the global Rayleigh damping matrix, the global stiffness matrix, and the global load vector of the electromagnetic interaction in the rail-vibration response analysis, respectively. The Rayleigh damping is proportional to a linear combination of the mass and stiffness. Mass-proportional and stiffness-proportional damping can be used separately. The stiffness-proportional damping is used in this study, because the stiffness-proportional damping can represent the internal material damping [52]:

$$\mathbf{C} = \lambda \mathbf{K}, \lambda = 2\eta/\omega_n, \quad (21)$$

where ω_n is the natural frequency, and η is the damping ratio and is taken as 0.04."

$$M = EI_m \frac{\partial^2 w}{\partial x^2}, Q = EI_m \frac{\partial^3 w}{\partial x^3}. \quad (22)$$

$$\sigma = \frac{M}{W}, \varepsilon = \frac{\sigma}{E} \left(W = \frac{bh^2}{6} \right) \quad (23)$$

When the rail deflection is obtained by solving Eq. (20), the bending moment M and the shear force Q can be given by Eq. (22), and the stress σ and strain ε can be given by Eq. (23).

2.3. Model implementation

In the model, the total numbers of rail elements are equal to the numbers of time steps to facilitate the numerical solution. The length of every rail element is identical, but the corresponding time step may not be. Consequently, the average speed associated with every rail element is obtained by dividing the length of every element by the corresponding time step. The magnetic pressure applied behind the armature extends from the breech to the muzzle in the railgun. Eq. (20) used for a rail vibration is solved using the Newmark method after Eq. (9) describing the armature motion is solved using the Runge–Kutta method.

The main computation steps of the Newmark method are briefly introduced as follows:

1. Generate the global mass matrix \mathbf{M} , the stiffness matrix \mathbf{K} , the damping matrix \mathbf{C} , and the load vector of electromagnetic interaction $\mathbf{q}(t, \mathbf{w}(t))$.
2. Determine the initial value of $\mathbf{w}(0)$, $\dot{\mathbf{w}}(0)$, and $\ddot{\mathbf{w}}(0)$.
3. Specify the integral parameters β and γ introduced in the Newmark method for the numerical computation, where γ is 0.5 and β is 0.25
4. Calculate the integral constant $b_1 \sim b_6$, where τ is the time step.

$$b_1 = \frac{1}{\beta\tau^2}, b_2 = \frac{1}{\beta\tau}, b_3 = -\left(\frac{1}{2\beta} - 1\right)$$

$$b_4 = \gamma b_1\tau, b_5 = 1 + \gamma b_2\tau, b_6 = (1 + \gamma b_3 - \gamma)\tau$$

5. Generate the effective stiffness matrix $\tilde{\mathbf{K}} = \mathbf{K} + b_1\mathbf{M} + b_4\mathbf{C}$.
6. Calculate the effective magnetic pressure at the moment $t + \tau_i$.

$$\tilde{\mathbf{q}}(t + \tau_i) = \mathbf{q}(t + \tau_i) + \mathbf{M}[b_1\mathbf{w}(t) - b_2\dot{\mathbf{w}}(t) - b_3\ddot{\mathbf{w}}(t)] + \mathbf{C}[b_4\mathbf{w}(t) - b_5\dot{\mathbf{w}}(t) - b_6\ddot{\mathbf{w}}(t)]$$

7. Calculate the deflection at the moment $t + \tau_i$.

$$\mathbf{w}(t + \tau_i) = \tilde{\mathbf{K}}^{-1} \tilde{\mathbf{q}}(t + \tau_i)$$

8. Calculate the generalized speed and acceleration.

$$\dot{\mathbf{w}}(t + \tau_i) = b_4[\mathbf{w}(t + \tau_i) - \mathbf{w}(t)] + b_5\dot{\mathbf{w}}(t) + b_6\ddot{\mathbf{w}}(t)$$

$$\ddot{\mathbf{w}}(t + \tau_i) = b_1[\mathbf{w}(t + \tau_i) - \mathbf{w}(t)] + b_2\dot{\mathbf{w}}(t) + b_3\ddot{\mathbf{w}}(t)$$

9. Time step τ_i becomes τ_{i+1} , and turn to step 4, until the end of the launch.

3. Model verification

Firstly, the proposed model is degenerated to the case that the armature moves at a constant speed, in order to be compared with the analytical solution of the rail deflection. With the Fourier sine integral transformation and Laplace–Carson integral transformation, the analytical solution Eq. (24) of the rail-vibration Eq. (1) is obtained by Daneshjoo in the form of series [12], where $W(n, t)$ is the transformation of $w(x, t)$.

Table 1

Main parameters of the railgun rail for a comparison with the analytical solution.

Rail density	Rail length	Rail height	Rail width	Young's modulus
8900 kg/m ³	2.75 m	0.015 m	0.03 m	120 GPa
Foundation stiffness	Initial half distance		Moment of inertia for rail	
6.15 GPa	0.015 m		8.4375 cm ⁴	

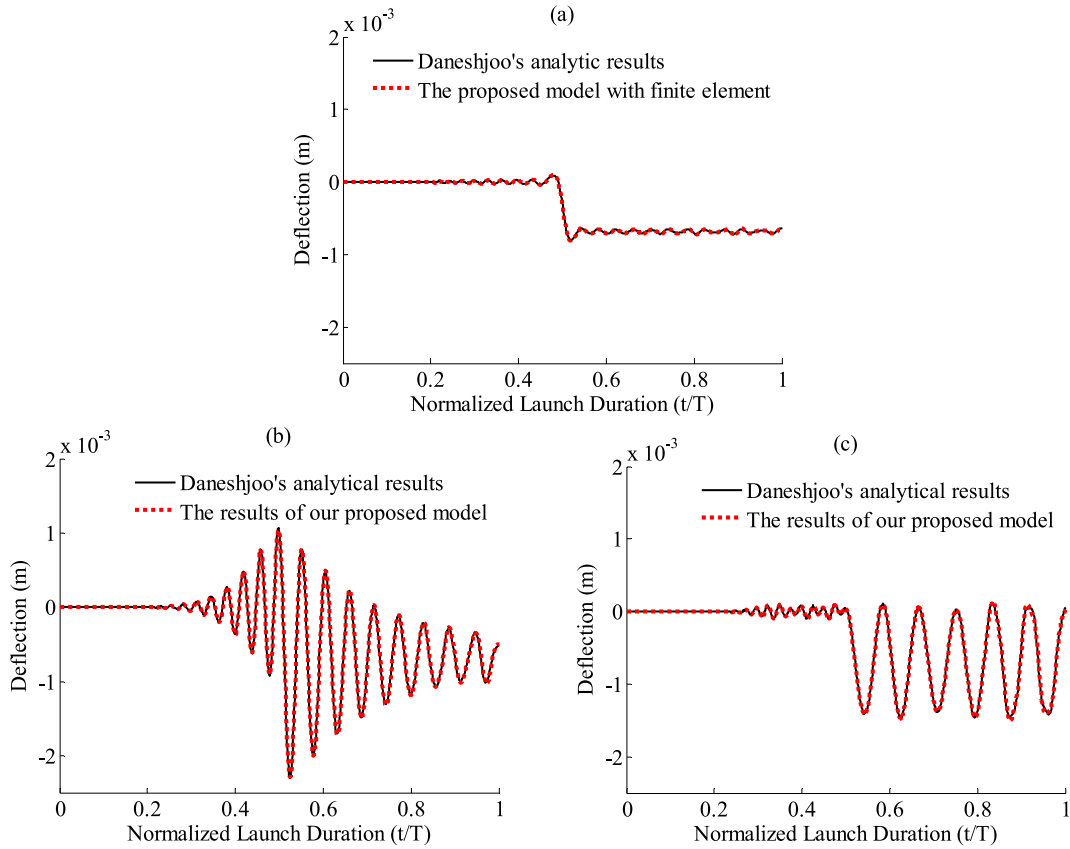


Fig. 3. Vibration response at the middle of the rail when the armature moves at a constant speed: (a) 800, (b) 1,145, and (c) 1500 m/s, T is the total time of railgun launch.

$$\begin{aligned}
 w(x, t) &= \frac{2}{L} \sum_{n=1}^{\infty} W(n, t) \sin\left(\frac{n\pi x}{L}\right) \\
 W(n, t) &= \frac{Q_n}{\lambda_n^2 \mu_n^2} \left[1 + \frac{1}{\lambda_n^2 - \mu_n^2} (\mu_n^2 \cos \lambda_n t - \lambda_n^2 \cos \mu_n t) \right] \\
 Q_n &= \frac{q n \pi v^2}{\rho A L}, \mu_n = \frac{n \pi v}{L}, \lambda_n = \left(\frac{k}{\rho A} + \frac{E I_m n^4 \pi^4}{\rho A L^4} \right)^{0.5}
 \end{aligned} \tag{24}$$

where q , ρ , A , L , E , I_m , and v in Eq. (24) are the magnetic pressure, rail density, rail cross-sectional area, rail length, Young's modulus, the moment of inertia for a rail, and the stiffness for the Winkler-type elastic foundation and the armature speed, respectively. The magnetic pressure is a constant value, and main parameters of the railgun rail are given in Table 1 for a comparison with the analytical solution.

$$V_{cr} = \left(\frac{4 E I_m k}{(\rho A)^2} \right)^{0.25} \tag{25}$$

The critical velocity V_{cr} was first derived from Eq. (1) by Timoshenko and is 1116 m/s at the same parameters shown in Table 1. The critical velocity is the lowest speed of naturally propagating bending waves and accompanied by the rail resonance [53]. Fig. 3 shows the vibration response at the middle of the rail (1.375 m) when the armature moves at a speed of 800, 1,145, and 1500 m/s, respectively. The vibration response of the analytical solution (solid black lines) is compared with the vibration response of our model's solution (dotted red lines). It can be seen that there is an excellent agreement between our proposed model predictions and Daneshjoo's analytical results, which could verify the reliability of the calculation. The amplitude of the vibration response is of the order of 10^{-4} to 10^{-3} m and a severe vibration response occurs when the

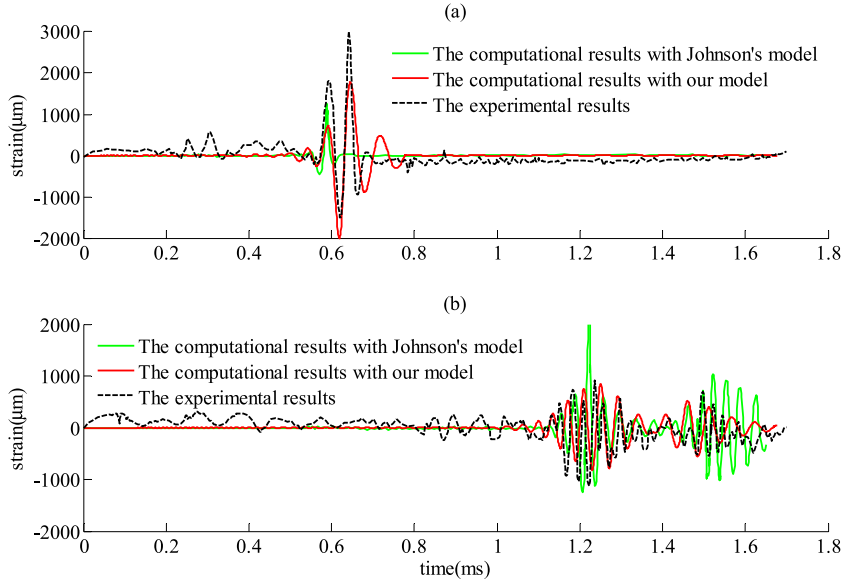


Fig. 4. Rail strain of experimental results and model predictions: the outside rail surface (a) 0.4 m and (b) 1.3 m from the initial position of the armature.

armature approaches the middle of the rail. The closer the armature is to the middle of the rail, the greater the vibration amplitude appears. The peak amplitude of the vibration response at the middle of the rail increases with the armature speed. When the armature speed is above the critical speed, the peak amplitude of the vibration response will no longer increase, although a strong wave radiation will be observed behind the moving load (Fig. 3c). The strong wave radiation is due to the moving loads exciting the rail vibration at the super-critical speed.

The predicted model is further validated through a comparison with the existing experimental data of the rail strain. Johnson experimentally measured the rail strain using the fiber Bragg grating strain sensors [47]. The strain gages were placed on the outside surface of a rail at 0.4 m (location 1) and 1.3 m (location 2) from the initial position of the armature. The main parameters of the experiment are as shown in Table 2.

The measured rail strains at locations 1 and 2 are shown with the dashed black lines in Fig. 4a and b and . The rail strains calculated by the proposed model are shown with the solid red lines, by substituting the rail deflection into Eq. (23). The solid green lines are the rail strains predicted by the Johnson's ANSYS model. The parameters used in our model are the same as those listed in Tables 2 and 3. It can be noticed that the amplitudes and distribution of rail strain predicted by the proposed model are well coincident with the experimental data both at locations 1 and 2, while the amplitudes of the rail strain predicted by Johnson's model are lower than the experimental results at location 1 and higher than the experimental results at location 2. Moreover, the distribution of rail strain predicted by Johnson's model is also not close to the experimental results. Good correspondence between the experimental observations and our model predictions may be due to the fact that the effect of the nonlinear dependence of the magnetic pressure on the rail deflection is considered through Eq. (6) in our model, but not considered in Johnson's model. There is a minor difference between our model prediction and the experimental data, and the reason may be the inability to completely avoid the electromagnetic interference noises during the experiment.

4. Results and discussions

4.1. Beam dynamics under different moving loads

The differences between the dynamics of rail beam under different moving loads are then compared. The case for single or periodic moving loads is obtained by simplifying the load of our proposed model. When the period T_0 of the periodic moving loads tends toward infinity it indicates a single moving load, and when T_0 tends toward zero it indicates an electromagnetic moving load. The displacement pattern of a rail deflection is given when the armature reaches the middle of the rail at a

Table 2

Main parameters of the experiment [47].

Rail length	Rail height	Rail width	Location 1	Location 2	Exit speed	Maximum current
1.5 m	0.0096 m	0.0189 m	0.4 m	1.3 m	≈ 1.2 km/s	≈ 0.273 MA

Table 3

Material properties [12,54] and the detailed values used in the proposed model.

Material density	Young's modulus	foundation stiffness
8320–8960 kg/m ³	115–130 GPa	4.15–6.15 GPa
8900 kg/m ³	120 GPa	5.8 GPa

Table 4

Parameters for armature motion during actual launch.

α	ξ_0	ω	γ_a	ρ_{air}
7622750 A	−1875	478	1.1	1.205 kg/m ³
A_b	C_f	p_f	L'	$F_{N,me}$
0.03 ² m ²	0	0	0.38 $\mu\text{H/m}$	3000 N

constant speed (see Fig. 5). Here the rail deflection is normalized because the levels of different moving loads cannot match. Evidently, the displacement pattern of rail deflection under an electromagnetic moving load differs greatly from that under a single or periodic moving load, while partially similar characteristics of the displacement pattern appear between the single and periodic moving load.

4.2. Different cases of the armature motion

Before discussing the rail vibration behavior in an actual launch, two simplified special cases of the armature motion which cannot be described using the proposed Eq. (9) are discussed. One involves armature moving at a constant speed with a constant magnetic pressure of 4.2 MPa applied on the rail (the vibration response at the middle of the rail, in this case, is shown in Fig. 3). The other involves armature moving with a varying acceleration with a constant magnetic pressure of 4.2 MPa applied on the rail. Although these two special cases are not closed to the actual railgun launch, they are also very helpful to understand the dynamic response of a rail beam under a moving load rapidly extending over the rail.

4.2.1. Constant speed

When the armature reaches different positions at a constant speed, the deflections along the rail have three displacement patterns. The rail deflections exhibit approximately a constant value profile behind the armature, but almost no deflection occurs ahead of it (Fig. 6a). For increased speed, the rail deflections firstly oscillate and increase from the rear of the rail, and then oscillate and decrease ahead of the armature (Fig. 6b). For even larger speed, the rail deflection shows approximately a sinusoidal distribution with little responses ahead of the armature (Fig. 6c). Fig. 6b shows that the wave trains under resonance develop behind the magnetic pressure front (armature position) at the speed slightly above the critical speed. Note that the rail deflections behind the armature in the cyan line differ from those of the other lines in Fig. 6b, which is due to the reflection or transition radiation of elastic waves. When the moving load come close and pass the rail end, the transition radiation can be caused by the load passing an inhomogeneity (e.g., the rail boundary) [55–57]. Fig. 6c shows that a nearly steady-state wave train develops behind the magnetic pressure front at super-critical speed. As a special feature of the deflection profile at a constant speed, the maximum deflection always occurs near the armature position.

In summary, the displacement patterns of the rail deflections under the electromagnetic moving loads can be attributed to the fact that the naturally propagating bending waves (wave trains) cannot develop at a speed (the speed of the moving load)

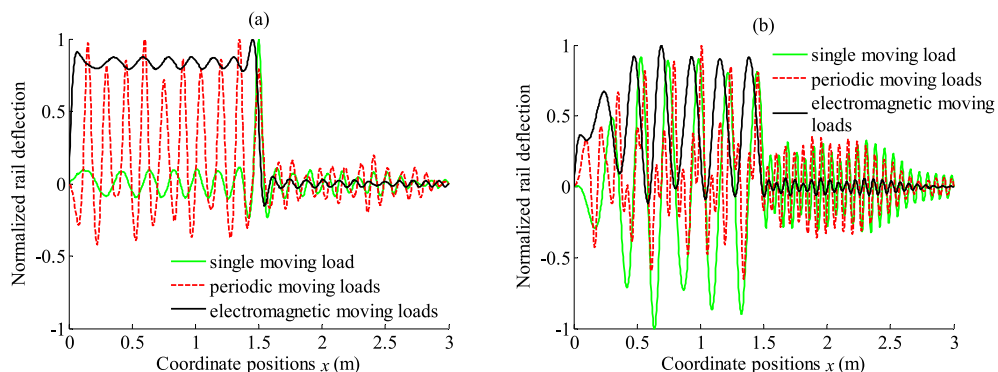


Fig. 5. Rail deflection when the armature reaches the middle of the rail under different moving loads at a constant speed: (a) 800 and (b) 1500 m/s.

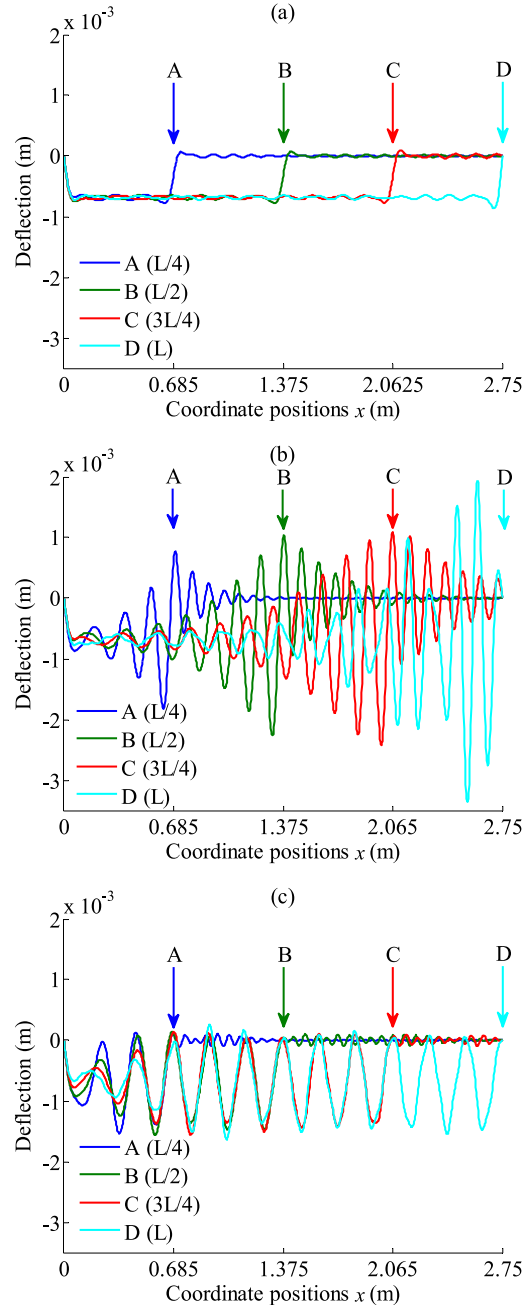


Fig. 6. Rail deflection when the armature reaches different positions (A: L/4; B: L/2; C: 3 L/4; D: L, where L is the rail length) at a constant speed: (a) 800, (b) 1,145, and (c) 1,500 m/s.

lower than the critical speed, but develop at a critical speed, and then continually develop at a super-critical speed (i.e., a strong wave radiation).

4.2.2. Varying acceleration

The varying acceleration is $a = l/\tau^2$, in which l is the length of the rail element and τ is the corresponding time step with the value of $\tau_i = 10^{-6}(1 - e^{(-i/500)})^{-1}$. In this case, the vibration responses at different locations of the rail (1/4 L, 1/2 L, and 3 L/4 of the rail, where L is the rail length) are shown in Fig. 7. The rail vibrations are mainly generated at the later stages of armature motion and the vibration frequency is stronger than that of the constant speed shown in Fig. 3. This is due to the magnetic pressure front (moving loads) travels along the rail with a lower initial speed at the initial time. However, during the

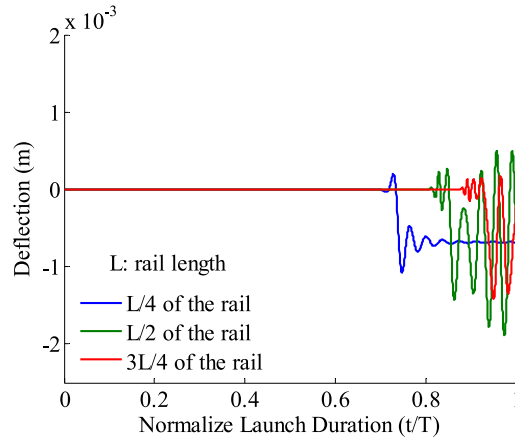


Fig. 7. Vibration responses at different locations of the rail when the armature moves with varying acceleration (L is the rail length; T is the total time of railgun launch).

later stages of armature motion, the magnetic pressure front (moving load) travels along the rail at a higher speed, even up to the super-critical speed.

When the armature reaches different positions with varying acceleration, the deflection along the rail is shown in Fig. 8. The rail deflections in the blue line are similar to the profile in Fig. 6a. As the distances that the armature travels increase, the rail deflection becomes similar to the profile in Fig. 6b, and finally similar to the profile in Fig. 6c. The armature speed (i.e., the speed of the magnetic pressure front) is slower than the critical speed at the initial time so that the rail deflection is similar to the cases at a low constant speed. However, when the speed under varying acceleration approaches the critical speed, the rail deflection shows a profile similar to the critical speed. Finally, the strong wave radiation also occurs at the super-critical armature speed. However, the rail deflection does not show a “steady-state” profile as compared to Fig. 6c, which is due to the influence of armature acceleration when the moving loads rapidly extend over the rail. The maximum deflection of the rail is far behind the armature position under varying acceleration.

In conclusion, the rail vibration shows approximately the displacement pattern of every phase of the constant speed in the case of a varying acceleration.

4.3. Actual launch

The rail vibration behavior is then discussed under an actual launch, in which the armature moves under a nonlinear pulse current. The parameters used are listed in Table 4. The time-dependent dynamic magnetic pressure behind the armature along the rail can be determined with Eq. (6). The nonlinear pulse current, electromagnetic force, frictional drag, and air drag are obtained using Eqs. (8) and (10)–(12), respectively. Fig. 9 shows that the air drag can be neglected compared to the electromagnetic forces and frictional drag. Substituting these forces into Eq. (9), the speed and acceleration can be obtained. The speed and acceleration without frictional drag are shown in the solid lines, and those with the frictional drag are shown in

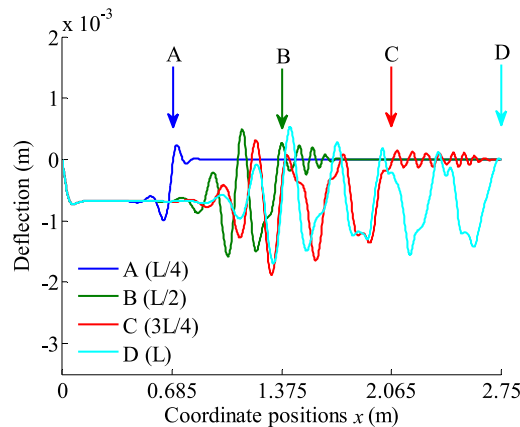


Fig. 8. Rail deflection when the armature reaches different positions (A: L/4; B: L/2; C: 3 L/4; D: L, where L is the rail length) with varying acceleration.

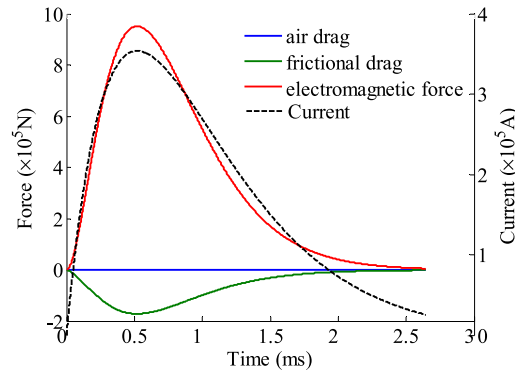


Fig. 9. Pulse current and forces acting on the armature.

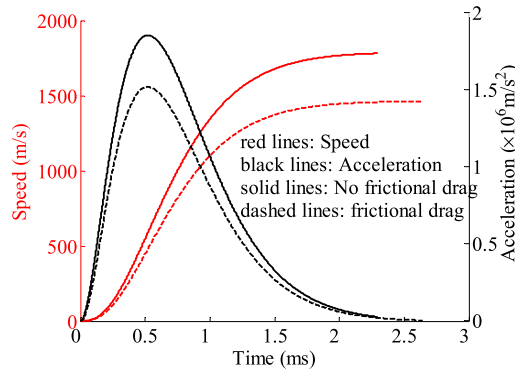


Fig. 10. Speed and acceleration of the armature.

the dashed lines. Fig. 10 indicates that the frictional drag significantly affects the speed and acceleration of the armature. The armature speed is reduced by 20% with the frictional drag taken into account. The smaller speed or acceleration will cause the magnetic pressure to be applied slower on the rails. The electrical energy introduced into the system is the same in both cases (with and without friction) at the same time. Therefore, due to the energy reduction by the frictional drag, the amplitude of the rail vibration with a frictional drag will be smaller compared to that without a frictional drag (see Figs. 11 and 12).

The comparison of the rail deflection between Figs. 11 and 12 shows that the smaller peak amplitude of deflection is generated when the frictional drag is considered. The deflection along the rail at a given time (1 ms and 2 ms) is shown in Fig. 13. The deflection along the rail with frictional drag (blue line) is smaller than that without frictional drag (red line). The

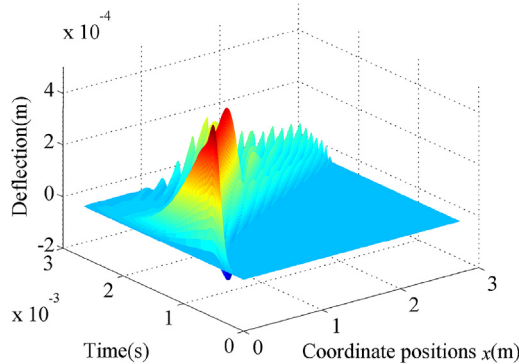


Fig. 11. Rail vibration response with frictional drag.

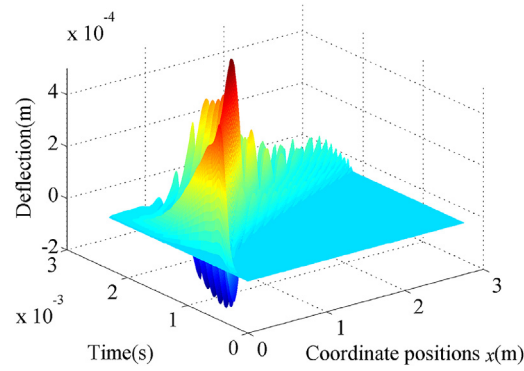


Fig. 12. Rail vibration response without frictional drag.

displacement patterns show that the deflection changes more dramatically, which indicates that the transient-state wave trains develop along the rail. The smaller amplitude of the rail deflection in the frictional case is due to the energy dissipation by the frictional drag.

The deflection profile in Fig. 13a is similar to that in Fig. 6b in the vicinity of critical speed. The elastic waves are then continually generated behind the magnetic pressure front, propagating forward along the rail. The influence of armature acceleration on rail deflection mentioned in Fig. 8 is also shown in Fig. 13b. In addition, the maximum deflection of the rail will be far behind the armature position during the actual launch (see the black and green dots in Fig. 13b). This is mainly because the armature speed accelerated by the electromagnetic force exceeds the critical speed when a nonlinear pulse current is applied, which causes the elastic wave to lag behind the armature motion.

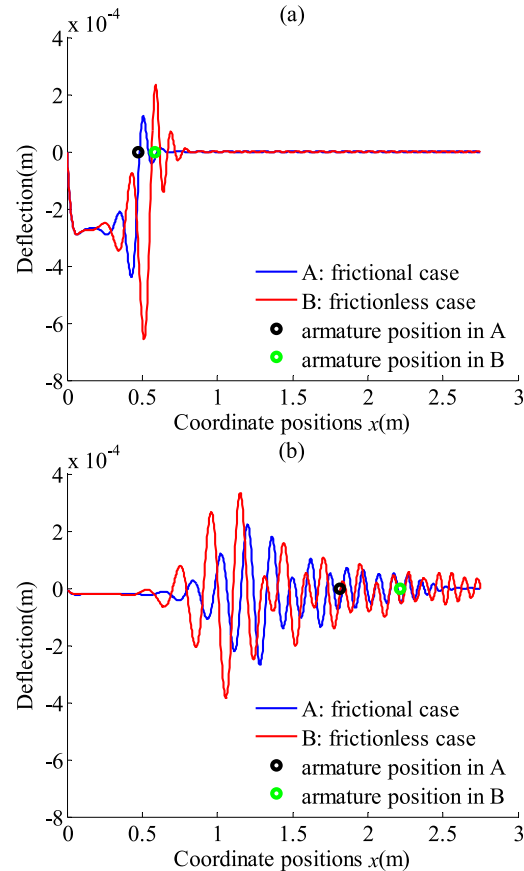


Fig. 13. Rail deflection at a given time: (a) 1 and (b) 2 ms

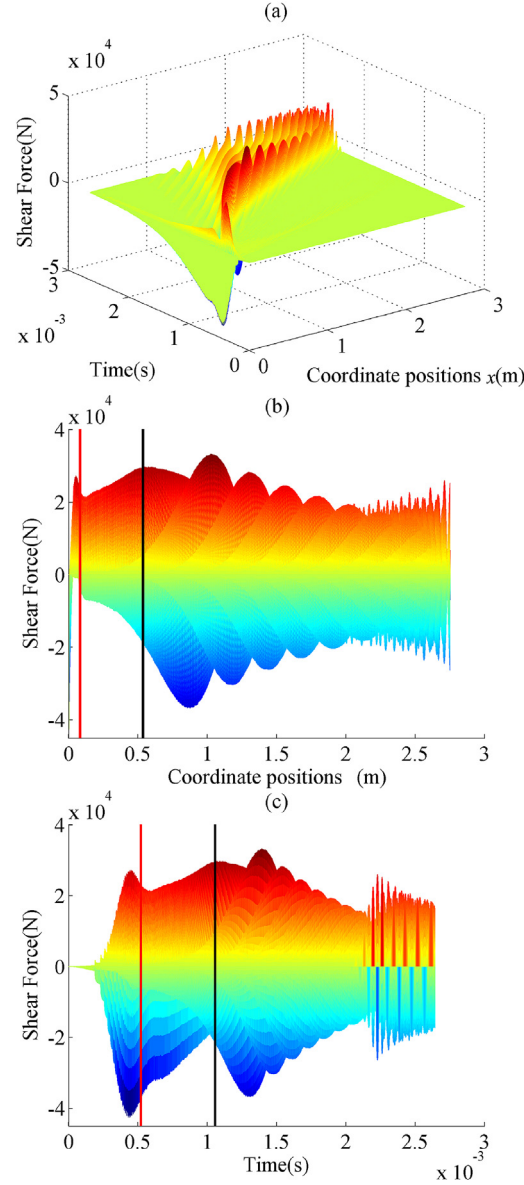


Fig. 14. (a) Shear force distribution during an actual launch. (b) projection of (a) onto SF-coordinate position plane; (c) projection of (a) onto SF-time plane

4.4. Shear force and bending moment

The shear force (SF) and bending moment (BM) both have a direct effect on the failure of the rail material. Once the rail deflection is obtained, the SF and BM are obtained through Eq. (22), as shown in Figs. 14 and 15, for an armature motion during an actual launch. For a clear illustration, the SF and BM in Figs. 14a and 15a are projected onto the planes along the axis of armature motion and along the time axis, respectively. The red lines correspond to the maximum pulse current at 0.084 m and 0.52 ms, and the black lines correspond to the critical speed at 0.537 m and 1.05 ms. Both the SF and BM have two maximum values along the rail, with the one in the initial part of the rail and the other between the 0.5 and 1 m (Figs. 14b and 15b), which refer to near 0.5 ms and between 1 and 1.5 ms in the time axis (Figs. 14c and 15c). The former maximum of the SF (or BM) is due to the fact that the pulse current reaches the maximum value at near 0.5 ms. The latter maximum of the SF (or BM) is due to the fact that the armature moves to the critical speed between 1 and 1.5 ms, accompanying the rail resonance. The maximum values of the SF and BM correspond to the most vulnerable fatigue areas. To avoid damage to the rail, the

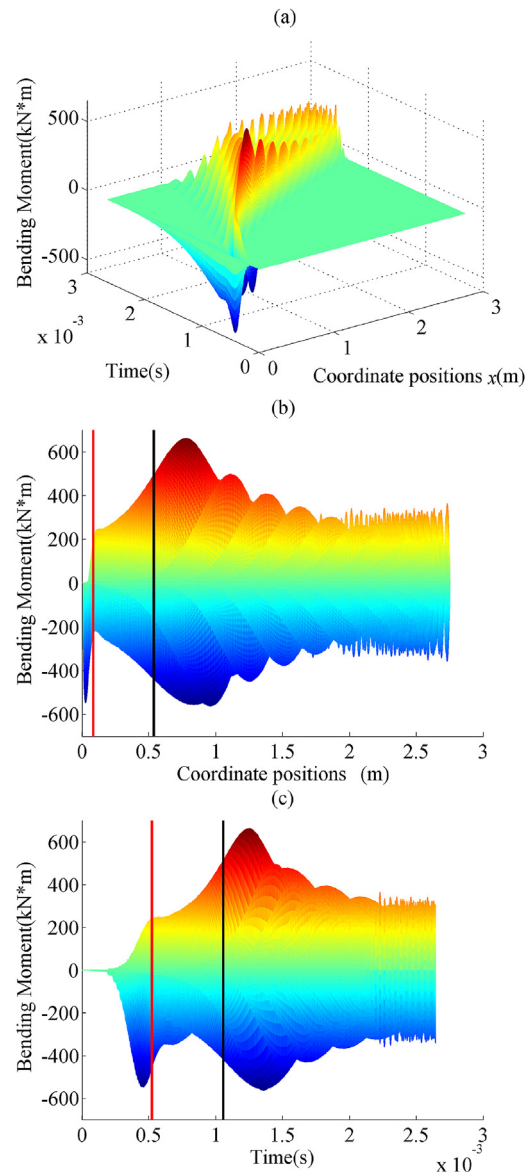


Fig. 15. (a) bending moment distribution during an actual launch. (b) projection of (a) onto BM-coordinate position plane. (c) projection of (a) onto BM-time plane

Table 5

Maximum error at different locations and pulse currents (L is the rail length).

	0.5 MA	1 MA	1.5 MA	2 MA	2.5 MA
1/4 L	1.86%	36.10%	48.46%	50.88%	68.98%
1/2 L	9.66%	16.49%	27.89%	26.04%	37.31%
3/4 L	5.72%	8.20%	14.94%	23.41%	23.46%

maximum armature speed must not exceed the critical speed. Or a high critical speed could be acquired based on the further railgun design.

4.5. Effect of the nonlinearity

We can ignore higher-order terms in the Taylor series expansion of magnetic pressure. Thus, the magnetic pressure can be given as:

$$\begin{aligned}
p(I(t), w) &= p_0(I(t)) + \left. \frac{\partial p}{\partial w} \right|_{w=0} w \\
p_0(I(t)) &= \frac{\mu_0 I^2}{\pi b} \left(\arctan \frac{b}{2r_0} + \frac{r_0}{b} \ln \frac{4r_0^2}{4r_0^2 + b^2} \right) \\
\left. \frac{\partial p}{\partial w} \right|_{w=0} &= \frac{\mu_0 I^2}{\pi b^2} \ln \frac{4r_0^2}{4r_0^2 + b^2}
\end{aligned} \tag{26}$$

When Eq. (26) is substituted into Eq. (1), we obtain the linearized governing equation (27) of the rail-vibration response.

$$\begin{aligned}
\rho A \frac{\partial^2 w}{\partial t^2} + EI_m \frac{\partial^4 w}{\partial x^4} + (k + k') w &= f' \\
k' &= - \left. \frac{\partial p}{\partial w} \right|_{w=0} (1 - H(x - \bar{x}))
\end{aligned} \tag{27}$$

$$\begin{aligned}
f' &= p_0(1 - H(x - \bar{x})) + F_N \delta(x - \bar{x}) \\
err &= ((\max w)_{NL} - (\max w)_L) / (\max w)_{NL}
\end{aligned} \tag{28}$$

Now, we can compare the response of the rail vibration associated with the linear and nonlinear forcing. The rail length is 3 m, and the other parameters are the same as in subsection 4.3. When the linear forcing through Eq. (27) and nonlinear forcing through Eq. (1) are considered, the maximum error of the rail deflection is given as Eq. (28), in which $(\max w)_{NL}$ is the maximum deflection with nonlinear forcing and $(\max w)_L$ is the maximum deflection with linear forcing. The maximum error at different locations (1/4 L, 1/2 L, and 3/4 L, where L is the rail length) and the pulse current (0.5, 1, 1.5, 2, and 2.5 MA) are shown in Table 5. Note that the effect of the nonlinearity is very important. The maximum error decreases with an increase in the rail location, and increases with the pulse current.

5. Conclusion

In this paper, a nonlinear finite element model was proposed to investigate the dynamic characteristics of a railgun under moving loads continuously extending over the rail. The moving loads were classified with armature motion in an actual launch and the special cases. These special cases include the armature moving at a constant speed and with a varying acceleration. The rail vibrations for a constant speed have three phases when the critical speed is considered. The naturally propagating bending waves (wave trains) along the rail cannot develop at a speed (the speed of the moving loads) lower than the critical speed, but develop at a critical speed, and then continues to develop into a steady-state pattern at a super-critical speed (i.e., a strong wave radiation). The vibration response for varying acceleration experiences all phases of a constant speed, and the armature acceleration will affect the rail vibration, in which transient wave trains develop along the rail. As a distinctive feature in the cases of an actual launch and varying acceleration, as compared to the case in constant speed, the maximum deflection of the rail will be far behind the armature position. In addition, the air drag can be neglected compared to the electromagnetic forces and frictional drag, and the armature speed is reduced by 20% with the frictional drag taken into account. More importantly, two maximums of the bending moment or the shear force on the rail occur. One occurs when the pulse current reaches the maximum value, and the other occurs when the armature approaches its critical speed. The two maximums should be considered in the further design of a railgun rail to avoid damaging the rails. A better understanding of such conclusions further improves the ability to design a railgun and provides knowledge on the dynamics of the beam under the moving loads that extend over the beam. In addition, when the armature is always in continuous contact with the rails and the stiffening effect in the support structure of railgun is weak, the dynamic instability induced by the effect of the armature inertia should be considered in a further detailed study.

CRediT authorship contribution statement

Bao Zhang: Software, Investigation, Data curation, Writing - original draft. **Yong Kou:** Validation, Formal analysis, Project administration, Funding acquisition. **Ke Jin:** Methodology, Writing - review & editing, Visualization. **Xiaoqing Zheng:** Conceptualization, Resources, Supervision.

Acknowledgments

This work was supported in part by the National Natural Science Foundation of China (Nos. 11872286, 11672217 and 11972272).

Appendix A. Effect of the insulator mass

The kinetic energy of railgun rail in length L can be present as follows:

$$E_{rail} = \frac{1}{2} \int_L \eta_r \left(\frac{\partial w(x, t)}{\partial t} \right)^2 dx, \quad (A.1)$$

where $\eta_r = \rho A$ is the mass per unit length of the rail, ρ is the rail density, and A is the cross-sectional area of the rail.

The foundation (insulator) is assumed to have a width b that is equal to the rail width shown in Fig. 2. Fig. A.1 shows the geometry of the foundation and rail, in which w_f is the deflection of the foundation at a distance z from the surface between the foundation and rail. The kinetic energy of the foundation in length L connecting to the rail can be presented as follows:

$$E_f = \frac{1}{2} \int_L \rho_f \left(\iint_{A_f} \left(\frac{\partial w_f(x, y, z, t)}{\partial t} \right)^2 dydz \right) dx, \quad (A.2)$$

where ρ_f is the insulator density and A_f is the cross-sectional area of the foundation.

The elastic foundation has the following:

$$\begin{aligned} z = 0, w_f(x, y, z, t) &= w(x, t) \\ z = H^*, w_f(x, y, z, t) &= 0, \end{aligned} \quad (A.3)$$

where H^* is the thickness of the foundation. Therefore, the velocity of the foundation at a distance z from the surface between the foundation and rail can be presented as follows:

$$\frac{\partial w_f(x, y, z, t)}{\partial t} = \frac{H^* - z}{H^*} \frac{\partial w(x, t)}{\partial t}. \quad A.4$$

Eq. (A.2) is then presented as follows:

$$E_f = \frac{1}{2} \int_L \eta_f \left(\frac{\partial w(x, t)}{\partial t} \right)^2 dx. \quad (A.5)$$

where $\eta_f = \rho_f A_f^*$ is the mass per unit length of the foundation.

$$A_f^* = \iint_{A_f} \left(\frac{H^* - z}{H^*} \right)^2 dydz \quad (A.6)$$

The total kinetic energy is as follows:

$$E = E_r + E_f = \frac{1}{2} \int_L (\eta_f + \eta_r) \left(\frac{\partial w(x, t)}{\partial t} \right)^2 dx. \quad (A.7)$$

This indicates that the effect of the mass of the insulator will increase the effective mass per unit length of the rail. The effective mass per unit length is as follows:

$$\eta_{eff} = \eta_f + \eta_r = \rho_{eff} A. \quad A.8$$

When the potential energy is given as Eq. (A.9) [58], which describes the work done by internal stress, external force f , and the foundation reaction kw , the Euler–Bernoulli beam Eq. (A.10) is obtained using Hamilton's variational principle.

$$U = \int_L \left(\frac{EI_m}{2} \left(\frac{\partial^2 w}{\partial x^2} \right)^2 + \frac{1}{2} kw^2 - fw \right) dx \quad (\text{A.9})$$

$$\rho_{\text{eff}} A \frac{\partial^2 w}{\partial t^2} + EI_m \frac{\partial^4 w}{\partial x^4} + kw = f(I(t), w) \quad (\text{A.10})$$

Eq. (A.10) is the same as Eq. (1) except for the meaning of the density. When the rail density (Cu Alloy) is 8320 kg/m^3 , and the insulator density (fiberglass or ceramic) is taken as $1557\text{--}1669 \text{ kg/m}^3$, the mass density 8900 kg/m^3 is a reasonably effective mass density in the railgun.

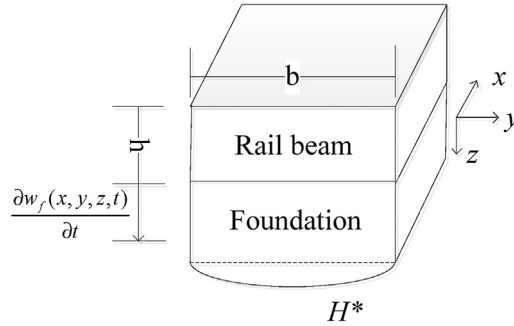


Fig. A.1. Geometry of the foundation and rail.

Appendix B. Weak nonlocality of the foundation response

In most cases, the interaction between the rail and insulator is presented by replacing the insulator with simple models of the elastic foundation, usually the Winkler model (spring elements). The Winkler model assumes that the foundation is represented as linearly elastic springs unconnected with each other. As the most important shortcomings of this model, the nonlocality of the response of the foundation is not considered (e.g., the interactions between the springs are not considered in the Winkler model). The nonlocality of the response indicates that, the foundation reaction at a given point, not only depend on the local value of the deflection, but also depend on that of neighbour points, with a distance-decaying effect [59]. We can consider the influence of the foundation response at neighbour points through the second-order derivatives of the deflection (i.e. weak nonlocality of the foundation response [60,61]). The foundation reaction will be represented as follows [62–64]:

$$Q_f = -k_1 w + k_2 \frac{\partial^2 w}{\partial x^2}, \quad (\text{B.1})$$

$$k_2 = \frac{GH}{2}. \quad (\text{B.2})$$

When the second term in the foundation reaction Q_f is ignored, the foundation reaction is the Winkler model. Here, k_1 is the same as k in Eq. (1), and k_2 is the interactions between the springs and takes the expression of Eq. (B.2) [65], where G is the shear modulus of the foundation and H is the thickness of the foundation. At this time, \mathbf{K}_2^e is added to the stiffness matrix.

$$\mathbf{K}_2^e = k_2 \begin{bmatrix} 6/5l & 1/10 & -6/5l & 1/10 \\ 1/10 & 2l/15 & -1/10 & -l/30 \\ -6/5l & -1/10 & 6/5l & -1/10 \\ 1/10 & -l/30 & -1/10 & 2l/15 \end{bmatrix} \quad (\text{B.3})$$

When the conditions described in subsection 4.3 are used and the shear modulus of the insulator is taken as 5.3 and 20 GPa, the vibration response of the middle of the rail is as shown in Fig. B.1. Clearly, the weak nonlocality of the foundation response has significant effect on the rail vibration at a larger shear modulus. When the insulator with an even larger shear modulus is used for a railgun, the nonlocality of the foundation response cannot be considered with Eq. (B.1) in an accurate manner, especially at very high speeds. At this time, the foundation reaction of a non-local foundation model should be considered through the kernel functions and the spatial integrations over the length of the foundation [66]. However, a non-local foundation model will be a systematic-comprehensive work for railguns, which needs a further research. Moreover, the

shear modulus of the insulator currently used in a railgun is small and the main problem is considered to be the analysis of the rail not the foundation. The simplest Winkler model is still used in this study owing to its easier use in engineering applications.

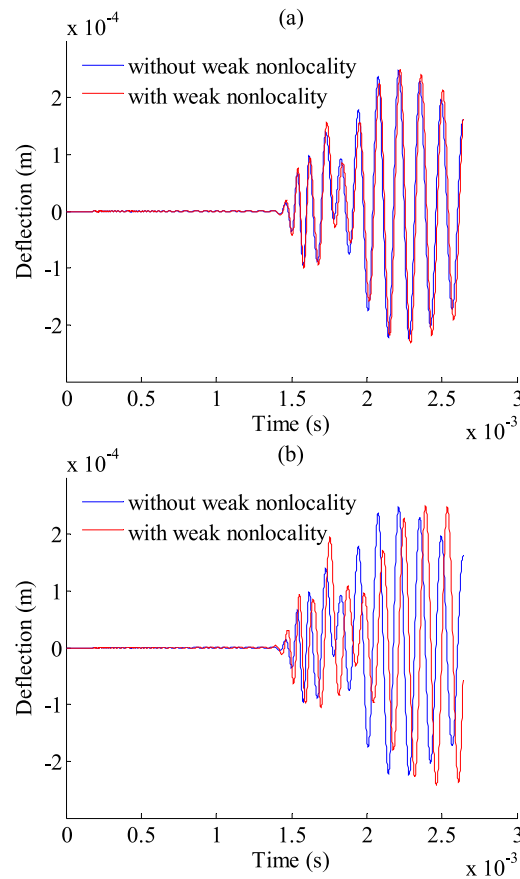


Fig. B.1. Vibration response of the middle of the rail with and without weak nonlocality: $G =$ (a) 5.3 and (b) 20 GPa.

References

- [1] I.R. McNab, F. Stefani, M.T. Crawford, M. Erengil, C. Persad, S. Satapathy, H. Vanicek, T. Watt, C. Dampier, Development of a naval railgun, in: Proceedings of 12th International Symposium on Electromagnetic Launch Technology (EML), Snowbird, Utah, 25–28 May 2004, pp. 76–80.
- [2] I.R. McNab, Progress on hypersonic railgun research for launch to space, IEEE Trans. Magn. 45 (2009) 381–388.
- [3] S. Hundertmark, Applying railgun technology to small satellite launch, in: Proceedings of 5th International Conference on Recent Advances in Space Technologies (RSAT2011), Istanbul, Turkey, 9–11 June 2011, pp. 747–751.
- [4] D. Micheli, A. Vricella, R. Pastore, R.B. Morales, M. Marchetti, Railgun application for high energy impact testing of nano-reinforced kevlar-based composite materials, in: Proceedings of 6th European Conference on Space Debris, Darmstadt, Germany, 22–25 April 2013, p. 208.
- [5] L.M. Barker, T.G. Trucano, A.R. Susoeff, Railgun rail gouging by hypersonic sliding contact, IEEE Trans. Magn. 25 (1989) 83–87.
- [6] F. Stefani, R. Merrill, Experiments to measure melt-wave erosion in railgun armatures, IEEE Trans. Magn. 39 (2003) 188–192.
- [7] J.P. Barber, D.P. Bauer, K. Jamison, J.V. Parker, F. Stefani, A. Zielinski, A survey of armature transition mechanisms, IEEE Trans. Magn. 39 (2003) 47–51.
- [8] T.J. Watt, The Onset of Gouging in High-Speed Sliding Contacts, PhD Thesis, UT Austin, Austin, Texas, 2011.
- [9] A.J. Johnson, T. Haran, F.C. Moon, W. Robinson, Stress wave measurements in an electro-magnetic launcher, in: Proceedings of 14th International Symposium on Electromagnetic Launch Technology (EML), Victoria, BC, Canada, 10–13 June 2008, pp. 1–6.
- [10] J.T. Tzeng, Dynamic response of electromagnetic railgun due to projectile movement, IEEE Trans. Magn. 39 (2003) 472–475.
- [11] J.T. Tzeng, W. Sun, Dynamic response of cantilevered rail guns attributed to projectile/gun interaction—theory, IEEE Trans. Magn. 43 (2007) 207–213.
- [12] K. Daneshjoo, M. Rahimzadeh, R. Ahmadi, M. Ghassemi, Dynamic response and armature critical speed studies in an electromagnetic railgun, IEEE Trans. Magn. 43 (2007) 126–131.
- [13] A.J. Johnson, F.C. Moon, Elastic waves and solid armature contact pressure in electromagnetic launchers, IEEE Trans. Magn. 42 (2006) 422–429.
- [14] A.J. Johnson, F.C. Moon, Elastic waves in electromagnetic launchers, IEEE Trans. Magn. 43 (2007) 141–144.
- [15] P.F. Pai, C.A. Kaufman, Characteristic speeds and influences of cross-sectional warpings on high-speed beam-foundation structures, Int. J. Mech. Sci. 59 (2012) 8–21.
- [16] N.V. Nechitailo, K.B. Lewis, Critical speed for rails in hypersonic launchers, Int. J. Impact Eng. 33 (2006) 485–495.
- [17] N.V. Nechitailo, K.B. Lewis, Influence of the critical speed on deformation of launcher components, Int. J. Impact Eng. 35 (2008) 1683–1687.
- [18] L. Tumonis, M. Schneider, R. Kacianauskas, V. Vadluga, The structural mechanics of railguns with discrete supports showing the influence of DES, IEEE Trans. Plasma Sci. 39 (2011) 144–148.
- [19] C. Schuppler, L. Tumonis, R. Kacianauskas, M. Schneider, Experimental and numerical investigations of vibrations at a railgun with discrete supports, IEEE Trans. Plasma Sci. 41 (2013) 1508–1513.

- [20] L. Tumonis, M. Schneider, R. Kačianauskas, A. Kačeniauskas, Comparison of dynamic behaviour of EMA-3 railgun under differently induced loadings, *Mechanika* 78 (2016) 31–37.
- [21] L. Xu, Y.B. Geng, Dynamics of rails for electromagnetic railguns, *Int. J. Appl. Electrom.* 38 (2012) 47–64.
- [22] Y.B. Geng, Dynamic response of rails for electromagnetic launcher with acceleration load, *Adv. Mater. Res.* 591 (2012) 2032–2036.
- [23] L. Frýba, *Vibration of Solids and Structures under Moving Loads*, vol. 1, Springer Science & Business Media, 2013.
- [24] M.A. Hilal, M. Mohsen, Vibration of beams with general boundary conditions due to a moving harmonic load, *J. Sound Vib.* 232 (4) (2000) 703–717.
- [25] M.A. Hilal, H.S. Zibdeh, Vibration analysis of beams with general boundary conditions traversed by a moving force, *J. Sound Vib.* 229 (2) (2000) 377–388.
- [26] M.A. Hilal, Vibration of beams with general boundary conditions due to a moving random load, *Arch. Appl. Mech.* 72 (9) (2003) 637–650.
- [27] G. Piccardo, F. Tubino, Dynamic response of Euler-Bernoulli beams to resonant harmonic moving loads, *Struct. Eng. Mech.* 44 (5) (2012) 681–704.
- [28] G.T. Michaltsos, Dynamic behaviour of a single-span beam subjected to loads moving with variable speeds, *J. Sound Vib.* 258 (2) (2002) 359–372.
- [29] P. Museros, E. Moliner, M.D. Martínez-Rodrigo, Free vibrations of simply-supported beam bridges under moving loads: maximum resonance, cancellation and resonant vertical acceleration, *J. Sound Vib.* 332 (2) (2013) 326–345.
- [30] M. Ichikawa, Y. Miyakawa, A. Matsuda, Vibration analysis of the continuous beam subjected to a moving mass, *J. Sound Vib.* 230 (3) (2000) 493–506.
- [31] Y.A. Dugush, M. Eisenberger, Vibrations of non-uniform continuous beams under moving loads, *J. Sound Vib.* 254 (5) (2002) 911–926.
- [32] Z. Oniszczuk, Forced transverse vibrations of an elastically connected complex simply supported double-beam system, *J. Sound Vib.* 264 (2) (2003) 273–286.
- [33] M.A. Hilal, Dynamic response of a double Euler–Bernoulli beam due to a moving constant load, *J. Sound Vib.* 297 (3–5) (2006) 477–491.
- [34] M. Kłasztorny, J. Langer, Dynamic response of single-span beam bridges to a series of moving loads, *Earthq. Eng. Struct. Dynam.* 19 (8) (1990) 1107–1124.
- [35] E. Savin, Dynamic amplification factor and response spectrum for the evaluation of vibrations of beams under successive moving loads, *J. Sound Vib.* 248 (2) (2001) 267–288.
- [36] A.V. Metrikine, K. Popp, Vibration of a periodically supported beam on an elastic half-space, *Eur. J. Mech. Solid.* 18 (4) (1999) 679–701.
- [37] A.V. Vostroukhov, A.V. Metrikine, Periodically supported beam on a visco-elastic layer as a model for dynamic analysis of a high-speed railway track, *Int. J. Solid Struct.* 40 (21) (2003) 5723–5752.
- [38] A.V. Metrikine, S.N. Verichev, J. Blaauwendraad, Stability of a two-mass oscillator moving on a beam supported by a visco-elastic half-space, *Int. J. Solid Struct.* 42 (3–4) (2005) 1187–1207.
- [39] S.M. Kim, Y.H. Cho, Vibration and dynamic buckling of shear beam-columns on elastic foundation under moving harmonic loads, *Int. J. Solid Struct.* 43 (3–4) (2006) 393–412.
- [40] A.K. Mallik, S. Chandra, A.B. Singh, Steady-state response of an elastically supported infinite beam to a moving load, *J. Sound Vib.* 291 (3–5) (2006) 1148–1169.
- [41] M. Ansari, E. Esmailzadeh, D. Younesian, Frequency analysis of finite beams on nonlinear Kelvin–Voight foundation under moving loads, *J. Sound Vib.* 330 (7) (2011) 1455–1471.
- [42] E.J. Sapountzakis, A.E. Kampitsis, Nonlinear response of shear deformable beams on tensionless nonlinear viscoelastic foundation under moving loads, *J. Sound Vib.* 330 (22) (2011) 5410–5426.
- [43] R. Zarfam, A.R. Khaloo, Vibration control of beams on elastic foundation under a moving vehicle and random lateral excitations, *J. Sound Vib.* 331 (6) (2012) 1217–1232.
- [44] H. Ding, L.Q. Chen, S.P. Yang, Convergence of Galerkin truncation for dynamic response of finite beams on nonlinear foundations under a moving load, *J. Sound Vib.* 331 (10) (2012) 2426–2442.
- [45] A.V. Metrikine, H.A. Dieterman, Instability of vibrations of a mass moving uniformly along an axially compressed beam on a viscoelastic foundation, *J. Sound Vib.* 201 (5) (1997) 567–576.
- [46] S.N. Verichev, A.V. Metrikine, Instability of vibrations of a mass that moves uniformly along a beam on a periodically inhomogeneous foundation, *J. Sound Vib.* 260 (5) (2003) 901–925.
- [47] A. Johnson, *Elastic Dynamics of Sliding Electrical Contacts under Extreme Conditions*, PhD Thesis, Cornell University Ithaca, New York, 2007.
- [48] M. Ghassemi, Y.M. Barsi, Effect of liquid film (indium) on thermal and electromagnetic distribution of an electromagnetic launcher with new armature, in: *Proceedings of 12th International Symposium on Electromagnetic Launch Technology (EML)*, Snowbird, Utah, 25–28 May 2004, pp. 386–392.
- [49] P. Lehmann, H. Peter, J. Wey, Experimental study of solid armatures for EML applications, *IEEE Trans. Magn.* 29 (1) (1993) 848–852.
- [50] Y.H. Lee, S.H. Kim, B.H. Lee, S. An, K.S. Yang, Experimental tests of a 25mm square-bore railgun, in: *Proceedings of 16th International Symposium on Electromagnetic Launch Technology (EML)*, Beijing, China, May 2012, pp. 15–19.
- [51] G.E. Rolader, J.H. Batteh, Effect of in-bore gas on railgun performance, *IEEE Trans. Magn.* 27 (1991) 120–125.
- [52] M. Petyt, *Introduction to Finite Element Vibration Analysis*, Cambridge university press, 2010.
- [53] K.B. Lewis, N.V. Nechitailo, Transient resonance in hypervelocity launchers at critical velocities, *IEEE Trans. Magn.* 43 (2007) 157–162.
- [54] J.R. Davis, *ASM Specialty Handbook: Copper and Copper Alloys*, ASM International, Metals Park, Ohio, USA, 2001. I-600 (2008).
- [55] A.I. Vesnitskii, A.V. Metrikine, Transition radiation in mechanics, *Phys. Usp.* 39 (10) (1996) 983.
- [55] Z. Dimitrova, A.F.S. Rodrigues, Critical velocity of a uniformly moving load, *Adv. Eng. Software* 50 (2012) 44–56.
- [56] A.B. Fărăgău, A.V. Metrikine, K.N. van Dalen, Transition Radiation in a Piecewise-Linear and Infinite One-Dimensional Structure—A Laplace Transform Method, *Nonlinear Dynam.*, 2019, pp. 1–27.
- [57] K.D. Hjelmstad, *Fundamentals of Structural Mechanics*, Springer Science & Business Media, 2007.
- [58] W. Flugge, *Viscoelasticity*, second ed., Springer-Verlag, Berlin, 1975.
- [59] A. Nobili, E. Radi, L. Lanzoni, A cracked infinite Kirchhoff plate supported by a two-parameter elastic foundation, *J. Eur. Ceram. Soc.* 34 (11) (2014) 2737–2744.
- [60] M. Cammarata, M. Zingales, Mechanical response of Bernoulli Euler beams on fractional order elastic foundation, in: *Proceedings of International Conference on Fractional Differentiation and its Applications (ICFDA 2014)*, Catania, Italy, 23–25 June 2014, pp1–6.
- [61] M.M. Filonenko-Borodich, Some Approximate Theories of Elastic Foundation, vol. 46, *Uchenyie Zapiski Moskovskogo Gosudarstvennogo Universiteta Mekhanika*, Moscow, 1940, pp. 3–18.
- [62] P.L. Pasternak, On a New Method of an Elastic Foundation by Means of Two Foundation Constants, *Gosudarstvennoe Izdatelstvo Literaturi po Stroitelstvu i Arkhitekture*, 1954.
- [63] V.Z. Vlasov, *Beams, Plates and Shells on Elastic Foundation*, Israel Program for Scientific Translation, 1966.
- [64] A.D. Kerr, On the determination of foundation model parameters, *Journal of Geotechnical Engineering* 111 (11) (1985) 1334–1340.
- [65] M.I. Friswell, S. Adhikari, Y. Lei, Vibration analysis of beams with non-local foundations using the finite element method, *Int. J. Numer. Methods Eng.* 71 (11) (2007) 1365–1386.